

論文 / 著書情報  
Article / Book Information

Title	Development of a frequency-detuned interferometer as a prototype experiment for next-generation gravitational-wave detectors
Authors	Kentaro Somiya, Peter Beyersdorf, Koji Arai, Shuichi Sato, Seiji Kawamura, Osamu Miyakawa
Citation	Applied optics, Vol. 44, , p. 3179
Pub. date	2005,
Copyright	Copyright (c) 2005 Optical Society of America
Note	<p>This paper was published in Applied optics and is made available as an electronic reprint with the permission of OSA. The paper can be found at the following URL on the OSA website: <a href="http://www.opticsinfobase.org/ao/abstract.cfm?uri=ao-44-16-3179">http://www.opticsinfobase.org/ao/abstract.cfm?uri=ao-44-16-3179</a> .</p> <p>Systematic or multiple reproduction or distribution to multiple locations via electronic or other means is prohibited and is subject to penalties under law.</p>

# Development of a frequency-detuned interferometer as a prototype experiment for next-generation gravitational-wave detectors

Kentaro Somiya, Peter Beyersdorf, Koji Arai, Shuichi Sato, Seiji Kawamura, Osamu Miyakawa, Fumiko Kawazoe, Shihori Sakata, Aya Sekido, and Norikatsu Mio

We report on our prototype experiment that uses a 4-m detuned resonant sideband extraction interferometer with suspended mirrors, which has almost the same configuration as the next-generation, gravitational-wave detectors. We have developed a new control scheme and have succeeded in the operation of such an interferometer with suspended mirrors for the first time ever as far as we know. We believe that this is the first such instrument that can see the radiation pressure signal enhancement, which can improve the sensitivity of next-generation gravitational-wave detectors. © 2005 Optical Society of America

OCIS codes: 120.2230, 120.3180, 120.5050, 350.1270.

## 1. Introduction

Gravitational-wave detection is the key to opening a new window of astronomy and is a door to still unknown new physics. The field was introduced in the early 20th century by Einstein, but a century later it is still one of the most challenging fields in physics. Since the signals from gravitational waves reaching the Earth are quite weak and there are a lot of undesirable noise sources, gravitational waves have not yet been directly detected. Indeed, with recent acceleration in the progress of technology, it will not be long before our scientific capabilities are sufficient for detecting gravitational waves.

Gravitational waves are perturbations to the met-

ric of space–time that travel through space. Reaching the Earth, the waves affect the relative displacement of free masses; hence the round-trip propagation time of light between any two free masses is changed. First-generation, gravitational-wave detectors such as TAMA,<sup>1</sup> the Laser Interferometer Gravitational Wave Observatory (LIGO),<sup>2</sup> and VIRGO (Ref. 3) employ the power-recycled, Fabry–Perot Michelson interferometer shown in Fig. 1. (GEO,<sup>4</sup> one of the first-generation detectors, has a different configuration as is mentioned below.) Gravitational waves increase the length of one Fabry–Perot arm cavity while they decrease the length of the other arm cavity. The reflected light fields from each arm cavity interfere at the beam splitter, and only the differential components leak through the signal-extraction port, which is otherwise kept dark to maximize the efficiency of the signal extraction. The rest of the light is reflected by the power-recycling mirror and reinjected to the interferometer so as to enhance the amount of light inside the cavities.

Since the magnitude of the displacements measured by gravitational-wave detectors on Earth is only  $10^{-20}$  m for kilometer-scale detectors, various kinds of noise can obscure detection, e.g., seismic motion, thermal perturbation, electronic noise. Among these, quantum fluctuation of the light in phase, so-called shot noise, is the most essential noise source. Quantum fluctuations of light are caused by a random walk in the photon number, which has individ-

---

When this research was performed, K. Somiya, P. Beyersdorf, K. Arai, S. Sato, and S. Kawamura were with the National Astronomical Observatory of Japan, 2-21-1 Osawa Mitaka-shi, Tokyo 181-8588, Japan. K. Somiya (somiya@hagi.k.u-tokyo.ac.jp) is now with the Max-Planck-Institut für Gravitationsphysik, Am Mühlenberg 1, 14476 Potsdam, Germany. O. Miyakawa is with the California Institute of Technology, Pasadena, California 91125. F. Kawazoe and S. Sakata are with Ochanomizu University, 2-1-1 Otsuka Bunkyo-ku, Tokyo 112-8610, Japan. A. Sekido is with Waseda University, 3-4-1 Okubo Shinjuku-ku, Tokyo 169-8555, Japan. N. Mio is with the University of Tokyo, 5-1-5 Kashiwanoha Kashiwa-shi, Chiba, 277-8562, Japan.

Received 14 July 2004; revised manuscript received 6 December 2004; accepted 19 December 2004.

0003-6935/05/163179-13\$15.00/0

© 2005 Optical Society of America

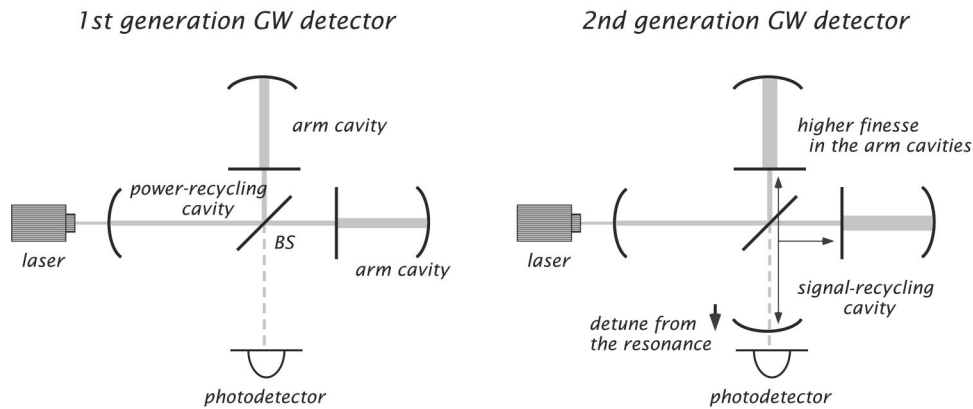


Fig. 1. Top, Power-recycled Fabry–Perot Michelson interferometer; bottom, power-recycled RSE interferometer: BS, beam splitter.

ual steps that are relatively small when the number of photons that may contribute to detecting a gravitational-wave signal are increased. Raising the circulation rate in the arm cavity, called finesse, is a way to raise the power of light and hence the signals, but, since high-frequency signals are canceled if the storage time is too high, the shot-noise level above the pole frequency of the cavity does not change with finesse. The use of an additional mirror placed at the dark port makes it possible to enhance the high-frequency signals and expand the observation band (Fig. 1, bottom). Although most of the light is recycled in the power-recycling cavity that is kept antiresonant for the carrier light, the signal component leaks out of the arm cavities through the signal-extraction cavity that is kept resonant for the carrier light. The signal-extraction cavity extracts and accumulates the high-frequency signals before they overcirculate in the arm cavity so that the sensitivity at frequencies higher than the cavity pole is improved. This technique, so-called resonant sideband extraction (RSE), was developed by Mizuno.<sup>5</sup>

The signal-extraction cavity can be kept in a non-resonant condition, or a detuned condition, so that the sensitivity spectrum is improved particularly at a

couple of frequencies as shown in Fig. 2. A signal at one particular frequency, which depends on the finesse of the arm cavities and the detuned phase of the signal-extraction cavity, resonates in the signal-extraction cavity or may be called a signal-recycling cavity, so that the amount of the signal is enhanced at that frequency. This causes the dip at the higher frequency. On the other hand, signals reflected by the signal-recycling mirror can be coupled with the incident carrier light at the beam splitter and then drive the arm-cavity lengths differentially by the light pressure, generating a signal at the same frequency. The resonant frequency of this chain reaction so-called optical spring,<sup>6</sup> which enhances the signal, depends on the finesse, detuned phase, signal-recycling gain, incident power, and the weight of mirrors in the arms. This causes the dip at the lower frequency, as further explained in Section 2.

Raising the power in the arm cavity not only decreases shot noise but also increases the radiation-pressure noise that results from quantum fluctuations in the photon number. The combination of these two aspects of quantum noise limits the sensitivity to be worse than what is called the standard quantum limit.<sup>7</sup> However, a detuned RSE interferometer can circumvent this rule owing to the radiation-pressure signal enhancement.

These two dips in the sensitivity spectrum due to detuning result in, for example, an overall 60% increase in the sensitivity to neutron star binaries, corresponding to a four-fold increase in the event rate. Second-generation detectors such as Advanced LIGO in the U.S.A. and the Large-Scale Cryogenic Gravitational Wave Telescope (LCGT) in Japan, operation of which is planned to start in approximately 2009, will employ RSE configurations, and their sensitivity will be limited by quantum noise over most of the spectrum, with a small band limited by thermal noise. The event rate of LCGT with detuning, for example, will be twice as high as that without detuning.<sup>8</sup>

It is clear in theory that detuning is effective in improving the sensitivity of second-generation, gravitational-wave detectors, but there are a couple

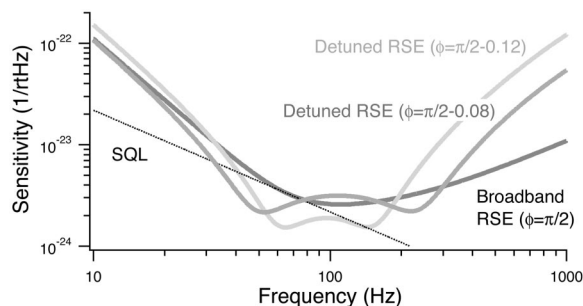


Fig. 2. Quantum-noise-limited sensitivity spectra of the detuned RSE interferometer. The spectra show a two-dip curve that can overcome the standard quantum limit, SQL. The spectra include only quantum noise. The baseline is 3 km, the test masses are 50 kg, the laser power is 1 kW at the beam splitter, the finesse of the arm cavities is 1250, and the amplitude reflectivity of the signal-recycling mirror is 0.96 for the detuned RSE and 0.82 for the broadband RSE.

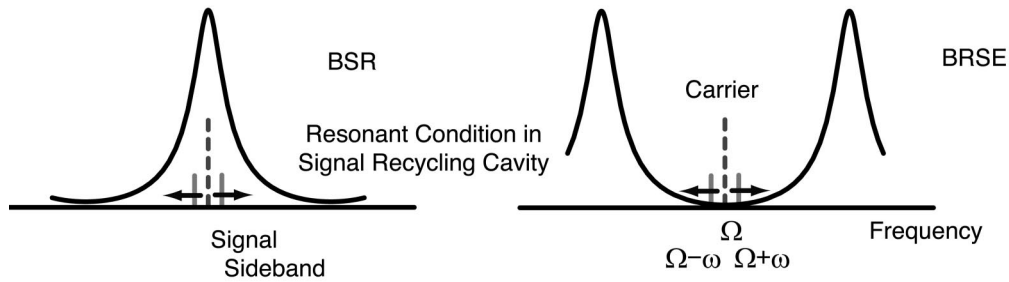


Fig. 3. Resonant condition of the signal-recycling cavity (SRC). Broadband signal recycling (BSR), enhances the signal sidebands at low frequencies, and the broadband RSE (BRSE) enhances the signal sidebands at high frequencies. The carrier light represented by the dashed line does not exist at the dark port.

of issues to be addressed before implementing the detuning in large-scale detectors, i.e., verification of the optical spring and establishment of the control scheme. So far, several table-top experiments with fixed mirrors have been demonstrated<sup>9–12</sup> but not with suspended mirrors. A control scheme proposed in previous experiments requires such a high-frequency modulation (180 MHz, more than 10 times higher than that of conventional detectors) for the control signal of RSE to be acquired that it may be troublesome in practice. Here we have developed the 4-m prototype detuned-RSE interferometer at the National Astronomical Observatory of Japan, and the experimental results are reported in this paper with the introduction of an alternative control scheme with a low-frequency modulation. This is the first successful operation of a signal-recycled Fabry–Perot Michelson interferometer with suspended mirrors and thereby the first trial for observing the effect of radiation-pressure signal enhancement.

After the mechanism of the broadband and detuned RSE configuration is explained in Section 2, our new control scheme is introduced in Section 3, and the experimental results of our prototype RSE interferometer is reported in Section 4.

## 2. Signal-Recycled Configurations

The dual-recycled Fabry–Perot Michelson interferometric configuration shown in Fig. 1 can be regarded as two coupled cavities: the power-recycled Fabry–Perot and the signal-recycled Fabry–Perot cavity. The carrier light is kept antiresonant in the power-

recycling cavity with no arm cavities assumed. The addition of arm cavities with the carrier light resonant flips the polarity of the compound mirror from that without arm cavities, and the resonant recycling cavity enhances the effective light power injected into the interferometer. When the signal-recycling cavity itself is antiresonant as well, the signal sideband around the carrier light is enhanced in the cavity, but the signal at high frequencies, being canceled in the cavity, is reduced. This condition is called broadband signal recycling. One can choose another signal-recycling condition in which the carrier light is antiresonant and the high-frequency signal is resonant. This condition is called broadband RSE.<sup>5</sup> Figure 3 shows the resonant condition of the signal-recycling cavity.

Raising the finesse, for example, by  $n$ , improves the shot-noise-limited sensitivity at frequencies lower than the cavity pole, thus decreasing the observation band by  $n$  while improving the floor level by  $n$  [Fig. 4(b)]. RSE degrades the floor level by  $\sqrt{n}$  while extending the observation band by  $n$  [Fig. 4(c)]. Therefore raising the incident power  $n$  times larger is equivalent to raising the finesse by  $n$  while extending the signal band by  $n$  by using RSE [Figs. 4(a) and 4(c)]. In both cases the cavity pole is kept constant, and the floor level is improved by  $\sqrt{n}$ . The signal-recycling mirror reflectivity required to realize the signal-band gain of  $n$  is

$$r_s = \frac{n-1}{n+1}. \quad (1)$$

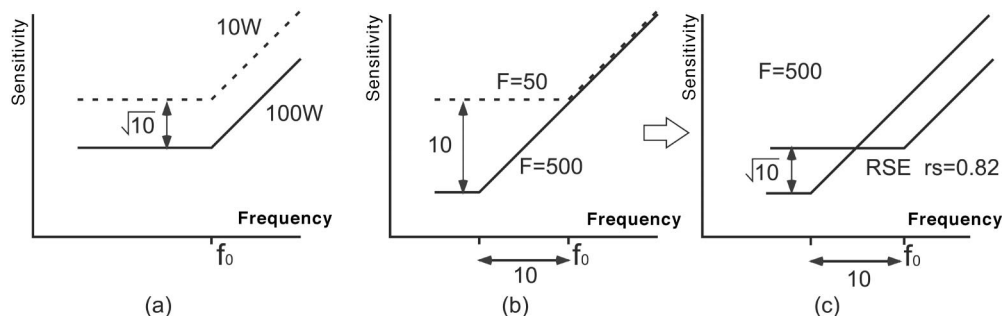


Fig. 4. Shot-noise-limited sensitivity improved (a) by raising the power or (b)–(c) by raising the finesse with RSE. Raising the incident power to be 10 times greater is equivalent to raising the finesse by 10 with extension of the signal band by 10 by using RSE.



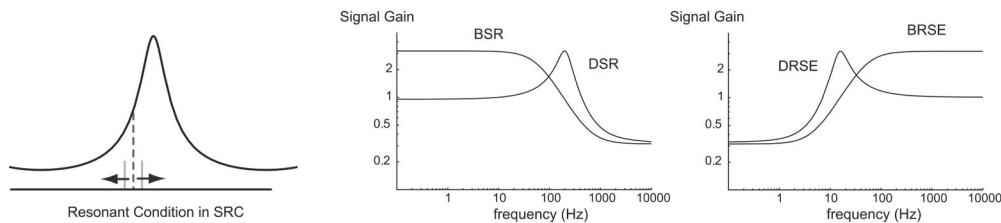


Fig. 5. Detuning the signal-recycling cavity enhancing the signal at an intermediate frequency. When the detuning phase is  $0 < \phi < \pi/4$  it is called detuned signal recycling, DSR, and when the detuning phase is  $\pi/4 < \phi < \pi$  it is called detuned RSE, DRSE.

For example, using laser power  $10\times$  higher is equivalent to using RSE with  $r_s = 0.82$  or  $R_s = 67\%$  in power reflectivity. Using  $100\times$  higher power is equivalent to RSE with  $R_s = 96\%$  mirror, which is not easy to realize in practice, considering the losses present in the Michelson interferometer. A combination of power recycling and RSE with the highest-power laser is recommended for enhancing the light power in the cavities.

Compared with a conventional, power-recycled, Fabry–Perot Michelson interferometer, a broadband RSE interferometer has a great advantage in terms of energy distribution.<sup>5</sup> The injected light power at the beam splitter necessary to make the same shot-noise level in each configuration is different. Although the Fabry–Perot Michelson interferometer does not require high-finesse arm cavities but rather high laser power, or a high-power-recycling gain, the RSE configuration enhances the light power in the high-finesse arm cavities instead of requiring high-power injection. The difference in the energy distribution results in a difference in the heating effect at the beam splitter and the front mirrors. Heating the optical substrates has many drawbacks such as a thermal lensing effect or cooling the mirrors.

So far only the resonant or antiresonant condition of the signal-recycling cavity is considered but not a nonresonant or detuned condition. In the detuned case one of the two signal sidebands approaches the resonance while the other recedes, and the total signal is enhanced at an intermediate frequency (Fig. 5). A detuned condition can be made by changing the signal-recycling cavity length from  $l_s$ , where dc components are antiresonant to  $l_s + \Delta l_s$ :

$$\frac{l_s \Omega}{c} = n\pi \quad (\text{broadband signal recycling}), \quad (2)$$

$$\frac{(l_s + \Delta l_s) \Omega}{c} = n\pi + \phi, \quad (3)$$

where  $\phi$  is defined as a detuned phase. Figure 6 shows the shot-noise spectra with various configurations, of which the detuned RSE shows the best sensitivity at a particular narrow frequency band.

The sensitivity curves shown here for detuned cases need to be modified with consideration of the radiation-pressure effect. While the output light from the broadband interferometer is phase-modulated signal sidebands and the reflected light from the signal-recycling mirror never couples to the incident laser beam to generate amplitude modulation, the output light from the detuned interferometer is unbalanced signal sidebands and the reflected light can couple to the incident beam to produce amplitude-modulated sidebands, which push the mirrors differentially owing to radiation pressure, generating more signal sidebands. This chain reaction results in the optical spring that can enhance the signal at its resonant frequency, even more than radiation pressure noise as shown in Fig. 2.

This effect was first theorized by Buonanno and Chen in 2000.<sup>6</sup> Although several table-top experiments with fixed mirrors have shown the signal enhancement of the higher-frequency peak in the response function of the interferometer that is responsible for the dip in the sensitivity curve,<sup>9–12</sup> the

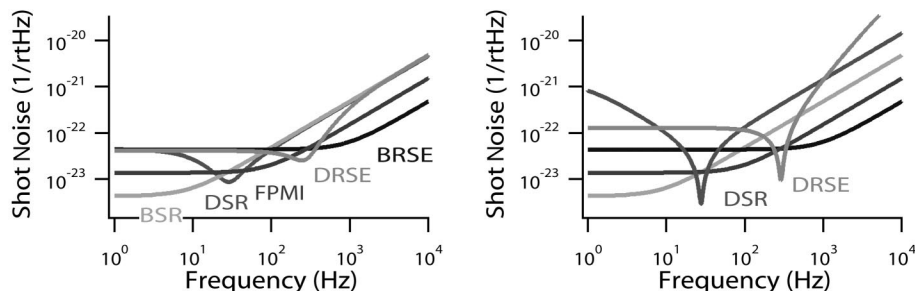


Fig. 6. Comparison of the shot-noise-limited sensitivity spectra with various configurations. The laser power is 50 W at the beam splitter, the finesse is 200, the arm length is 3 km, and the reflectivity of the signal-recycling mirror is, left, 67% for any configuration and, right, 96% for the detuned cases.

radiation-pressure signal enhancement of the lower-frequency peak that requires suspended mirrors that are free to respond to forces was not observed. The mirrors of GEO, the detuned signal-recycling interferometer without arm cavities, are suspended on pendulums, showing good results with regard to measurement of the peak at the higher frequency but not yet the peak at the lower frequency because the power at the mirror is not high enough without the arm cavities. Our group succeeded in 2001, in the operation of the prototype broadband RSE interferometer with suspended mirrors,<sup>13,14</sup> and our group has reconstructed the interferometer by using a new control scheme allowing for detuning of the signal-recycling cavity.

### 3. Length Sensing and Control of Resonant Sideband Extraction

The detuned RSE interferometer is much more promising than conventional detectors for detecting grav-

itational waves but is much more complex and has an additional degree of freedom to be controlled. Here we explain how to design the control scheme of the advanced interferometer and introduce our new control scheme that we recommend be adopted for second-generation interferometers.

signal while removing any dc offset, which can mix in the control signals  $\delta l_+$ ,  $\delta l_-$ , and  $\delta l_s$  in the case of a detuned interferometer.<sup>8</sup> This technique is called double demodulation.

The lengths between the beam splitter and the two front mirrors are different by  $\Delta l$  so that a fraction of the rf sidebands can leak through the dark port to beat with any carrier light at the dark port giving the  $\delta L_-$  signal. The transmission ratio of the upper and the lower sidebands in amplitude from the bright port through the dark port or vice versa is  $\pm i \sin \alpha$  with the asymmetry factor  $\alpha = \Delta l \omega_m / c$ , where  $\omega_m$  is the angular frequency of the rf modulation. The reflectivity from the bright (dark) port to the bright (dark) port is  $\cos \alpha$ .

The asymmetry factor can be used to maximize the signal-extraction efficiency of  $\delta l_s$  in the case of an RSE interferometer.<sup>8,15</sup> The sideband field at the bright port with the  $\delta l_s$  signal generated at the signal-recycling mirror is proportional to

$$-r_p + \frac{t_p^2 \{ (\cos \alpha - r_s) [1 + r_p r_s - (r_p + r_s) \cos \alpha] + i r_s \sin^2 \alpha \psi_s \}}{[1 + r_p r_s - (r_p + r_s) \cos \alpha]^2}, \quad (4)$$

where  $\psi_s$  represents the phase shift due to the motion of the signal-recycling mirror and  $t_p(t_s)$  and  $r_p(r_s)$  are the transmissivity and the reflectivity, respectively, of the power-recycling (signal-recycling) mirror in amplitude. Here we omit the net phase shift at the mirrors and express the reflectivity just as  $r_p(r_s)$  at the resonance and  $-r_p(-r_s)$  at the anti-resonance of the cavity. In Eq. (4) the coefficient of  $\psi_s$  is the signal-extraction efficiency of  $\delta l_s$ , which is maximized when

$$\cos \alpha = \frac{r_p + r_s}{1 + r_p r_s}. \quad (5)$$

The addition of the signal-recycling mirror requires another common-mode control for  $\delta l_s$ , and one shall implement the second modulation to control all 5 degrees of freedom. The common-mode signal for the arm cavities, that is,  $\delta L_+$ , is controlled by taking the beat of the carrier and the sidebands at  $f_1$  (or  $f_2$ ), while the other two common-mode signals are controlled by taking the beat between two sidebands. This two-frequency modulation scheme makes it possible to isolate the great significance of  $\delta L_+$  and  $\delta L_-$  from the control signal of the central dual-recycling interferometer. In addition, demodulating by  $f_1$  and  $f_2$  in series instead of demodulating by  $f_1 - f_2$  at once, one can choose two demodulation phases to maximize the

The first modulation sidebands  $f_1$  do not need to leak through the dark port while the second sidebands  $f_2$  need to leak to detect the  $\psi_s$  signal. Without power recycling ( $r_p = 0$ ) Eq. (5) has two solutions: one for  $r_s > 0$  and the other for  $r_s < 0$ . Although the former seems usual and is available when the signal-recycling cavity is in resonance, the latter is also available when the signal-recycling cavity is antiresonant for the sidebands at  $f_2$ . With power recycling Eq. (5) also has two solutions: one is a smaller asymmetry factor with both the recycling cavities resonant, and the other is a larger asymmetry factor with either recycling cavity antiresonant. We call the former one the low-low method and the latter one the low-high method (see Fig. 7).

The low-high method was developed for Advanced LIGO, where  $f_1$  is 9 MHz and  $f_2$  is 180 MHz. In this method, when  $r_p \approx r_s$ , the asymmetry is approximately  $\pi/2$ , the incident sidebands at  $f_2$  transmit to

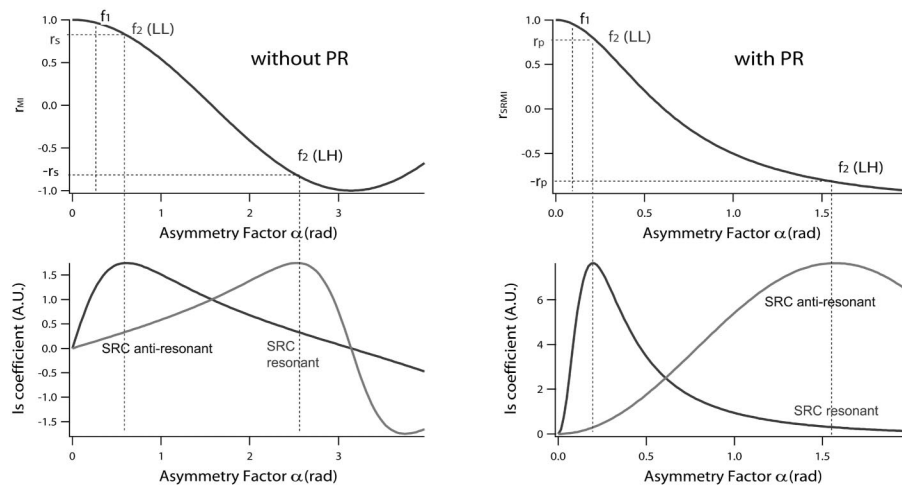


Fig. 7. Coefficient of the  $\psi_s$  signal in Eq. (4) maximized when the reflectivity of the Michelson interferometer in the case without power-recycling matches  $\pm r_s$  or the reflectivity of the signal-recycled Michelson interferometer in the case with power recycling matches  $\pm r_p$ .

the dark port, and all the light reflected by  $r_s$  returns to the bright port with the information of  $\psi_s$ .<sup>16</sup> The sidebands at  $f_2$  are not resonant in the power-recycling cavity but are resonant in the coupled cavity of dual recycling. The two frequencies  $f_1$  and  $f_2$  are well separated for a couple of reasons: to avoid an interaction from the harmonics and to make  $\alpha$  for the sidebands at  $f_1$  so small that other degrees of freedom controlled by the sidebands at  $f_1$  are not affected by the signal-recycling cavity (Fig. 8).

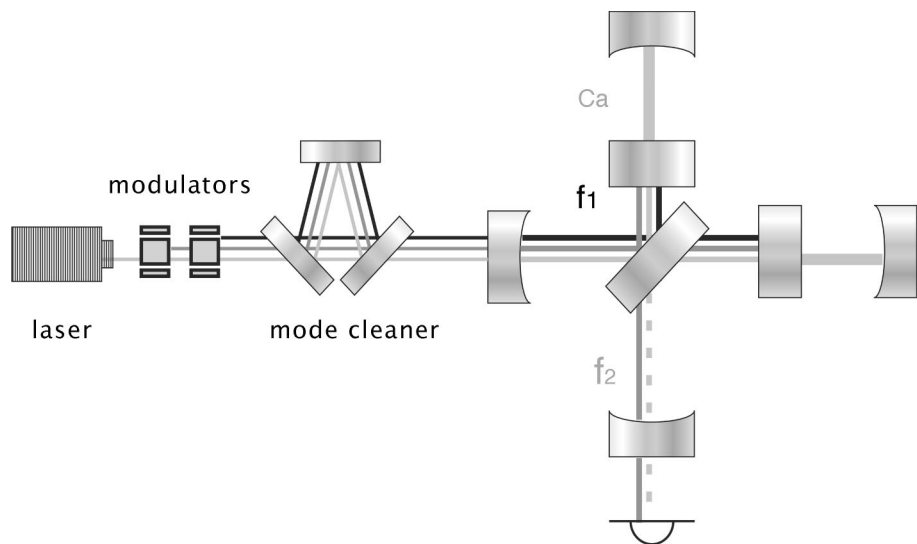
The only weakness of this model is that either one of the sidebands at  $f_2$ , which resonates in the dual-recycling cavity and is used to detect  $\delta L_-$ , is so high in frequency as to cause several practical problems. One such problem is that the phase noise of the modulator would be increased and the efficiency of the  $\delta L_-$  photodetector would be decreased. To avoid this problem, Advanced LIGO employs a dc readout scheme by which the sideband at  $f_2$  is not used as the local oscillator to detect  $\delta L_-$ , but instead the dc light present from being locked slightly off the dark fringe plays the role of the local oscillator.<sup>17</sup> Compared with the conventional rf readout scheme, the dc readout scheme has many advantages but with increased complexity.

The low-low method had not been sufficiently discussed for use in a high-sensitivity detector before we found the appropriate scheme. A concern was that the harmonics of the sidebands at  $f_1$  might have a strong effect on the signal obtained by the sidebands at  $f_2$ . If one can deal with the harmonics somehow, the low-low method would be advantageous because  $f_2$  is relatively low even with little asymmetry. One solution is to set  $f_2$  not to be an integer multiple of  $f_1$  but a common multiple of the free-spectral range of the power-recycling cavity with  $f_1$ . Then the influence of harmonics is not troublesome even if the two modulation frequencies are as close as 15 and 35 MHz, where the free-spectral range of the power-recycling cavity is 10 MHz.

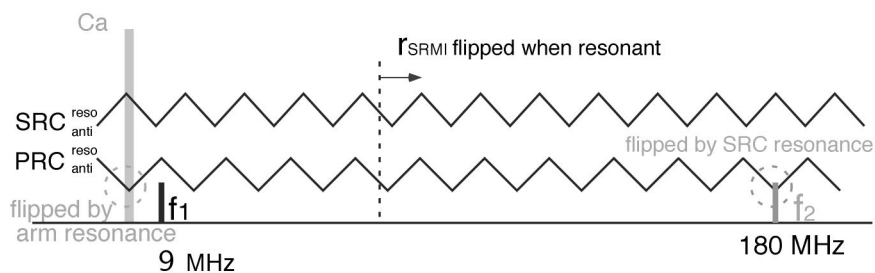
Table 1 shows that both methods have almost the same efficiency (the signal level for the same value of the laser power and the modulation depth of the rf sidebands) in extracting the control signals either in the broadband cases or in the detuned cases. These are the calculated results with the simulation software FINESSE.<sup>18</sup> For the broadband case the sidebands at  $f_1$  are amplitude modulation and those at  $f_2$  are phase modulation. This arrangement makes the amplitude of the beat signal between the sidebands sensitive to the phase of the sidebands at  $f_2$  relative to those at  $f_1$ . The  $\delta L_+$  signal is taken at the pickoff port by  $f_2$  for the broadband cases and at the bright port by  $f_1$  for the detuned cases. The  $\delta L_-$  is taken at the dark port by  $f_2$ . The  $\delta l_+$ ,  $\delta l_-$ , and  $\delta l_s$  are taken at the bright port, the dark port, and the pickoff port, respectively, by double demodulation. The amount of the signal taken at the pickoff port should be multiplied by the reflectivity of the pickoff mirror. Although the units for these numbers are arbitrary, it is clear that the amount of each control signal is almost the same between the low-low and low-high methods.

The signal-recycling cavity can be locked to a detuned condition for the carrier light when only one of the upper and the lower  $f_2$  sidebands resonates in the cavity with the free-spectral range longer or shorter than that for the broadband condition. The detuned phase should be chosen to optimize the sensitivity to expected gravitational waves. For example, the sensitivity of LCGT for the gravitational waves from the neutron star binaries is maximized with the detuned phase of 0.12 from the broadband RSE condition, which requires the rearrangement of the signal-recycling mirror by 16 cm with the 15–35-MHz control scheme.

There is one small difference between the low-low method and the low-high method when the signal-recycling cavity is detuned. In the former case, when the  $+f_2$  sideband is resonant in the dual-recycling



9–180 MHz model



15–35 MHz model

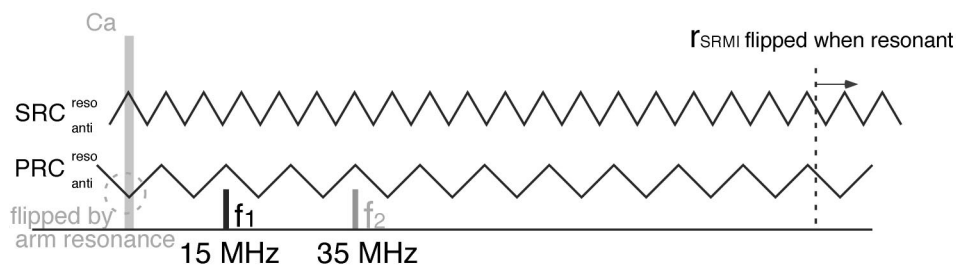


Fig. 8. Resonant condition of the low–high and the low–low method. The sign of the reflectivity of the signal-recycled Michelson interferometer is flipped above a particular frequency determined by the asymmetry length. The power-recycling cavity is antiresonant for 180-MHz sidebands, but the resonant condition of the signal-recycling cavity that is originally resonant for 180-MHz sidebands is flipped to antiresonant so that the total dual-recycling cavity is resonant.

cavity, the  $-f_2$  sideband is also resonant in the power-recycling cavity, while in the latter case, when  $+f_2$  is resonant in the dual-recycling cavity,  $-f_2$  is nonresonant in any cavities. The low–high method in a detuned condition provides greater sensitivity to  $\delta l_+$  than the low–low method in a detuned condition or either method in the broadband condition, since the nonresonant sideband in the detuned configuration with the low–high method avoids signal cancellation with the resonant sidebands.

Table 2 shows the signal-extraction matrix with the 15–35-MHz control scheme. The components are

normalized so that the diagonal elements are unity. In this matrix all off-diagonal elements are less than unity, and in particular the components on the line of  $l_-$  extraction are sufficiently small, so that the only path that contributes to  $L_-$ , through  $l_-$ , is well isolated from the other signals that could introduce excess noise.

Finally, we recommend that the 15–35-MHz scheme be adopted for the second-generation interferometers. In Section 4 we demonstrate a prototype RSE experiment for which the control scheme based on the 15–35-MHz model has been used.



**Table 1. Signal Amount Calculated by the Simulation**  
Software FINESSE

Degrees of Freedom, Length	$\delta L_+$	$\delta L_-$	$\delta l_+$	$\delta l_-$	$\delta l_s$
9–180-MHz broadband	7140	261	0.064	0.018	0.273
15–35-MHz broadband	8760	265	0.050	0.018	0.281
9–180-MHz detuning	3190	71	0.154	0.009	1.399
15–35-MHz detuning	3190	71	0.053	0.009	1.434

Note:  $r_p = 0.8485$  and  $r_s = 0.8246$  are in the broadband case, whereas  $r_s = 0.96$  is in the detuning case, and the asymmetry factor is optimized for each case. The free-spectral range of the power-recycling cavity is 18 MHz for the 9–180-MHz model and 10 MHz for the 15–35-MHz model, and that of the signal-recycling cavity is 180/11 MHz for the 9–180-MHz model and 35/6 MHz for the 15–35-MHz model. As for the detuning, the length of the signal-recycling cavity is changed by 3 cm for the 9–180-MHz model and 16 cm for the 15–35-MHz model to detune the interferometer by 0.12 rad.

#### 4. Prototype Experiment

##### A. Experimental Setup

We constructed our 4-m prototype interferometer at the National Astronomical Observatory of Japan. The arm cavities, the beam splitter, and the signal-recycling mirror are placed inside the vacuum cham-

bers to avoid losses caused by gas and dust. The performance of the chambers is  $1.0 \times 10^{-6}$  Torr with the optics inside.

Figure 9 shows a schematic view of the interferometer. Three rf photodetectors are necessary to extract the control signal of the interferometer: the bright port photodetector for  $\delta l_-$  and  $\delta l_s$  and the pickoff port photodetectors for  $\delta L_1$  and  $\delta L_2$ . A better signal-to-noise ratio could surely be achieved by taking the  $\delta L_-$  signal from the dark port, but the signal from the subtraction of  $\delta L_1$  and  $\delta L_2$  with careful adjustment of the control gain for two arm cavities is sufficient and much easier to implement; so it is used. At the dark port the optical-spectrum analyzer is set up for the resonant condition of each sideband to be seen. Inside the chambers are a number of steering mirrors and six core optics: the signal-recycling mirror ( $R = r^2 = 80\%$ ), the beam splitter ( $R = T = 50\%$ ), the front mirrors ( $R = 99.7\%$ ), and the end mirrors ( $R = 99.99\%$ ). All the mirrors are suspended by a one-loop single pendulum with an eddy-current damping system. The arm-cavity length is 3.8 m.

##### B. Transfer Function of Resonant Sideband Extraction

The transfer function of the interferometer can be derived by taking the ratio of the gravitational-wave

**Table 2. Signal-Extraction Matrix with the 15–35-MHz Model Control Scheme for the Detuned RSE Interferometer**

Signal Extraction	Demod.	$L_+$	$L_-$	$l_+$	$l_-$	$l_s$
Symmetric port	$f_1$	1	0.000	−0.000	0.000	−0.000
Antisymmetric port	$f_2$	0.000	1	0.000	0.001	0.000
Symmetric port	DDM <sup>a</sup>	0.000	−0.001	1	0.495	0.698
Antisymmetric port	DDM <sup>a</sup>	−0.000	0.002	−0.009	1	−0.015
Pick-off port	DDM <sup>a</sup>	0.002	−0.002	0.033	−0.894	1

<sup>a</sup>Double demodulation by  $f_1$  and  $f_2$ . The components are normalized so that the diagonal sections are unity.

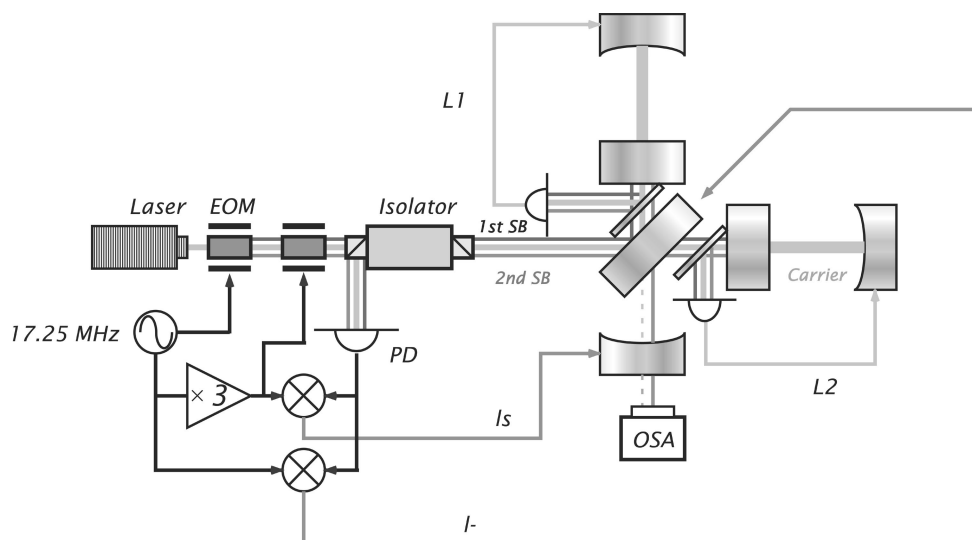


**Fig. 9. Schematic view of the 4-m prototype RSE experiment.** In addition to the first main modulator the secondary modulator is used to eliminate the third harmonics. The control signals for the Michelson interferometer and the signal-recycling mirror are obtained from the light at the bright port, and the control signals for the arm cavities are obtained from the reflected light from the pickoff mirrors located between the front mirrors and the beam splitter: EOM, electro-optic modulator; PD, photodetector; SB, sideband.

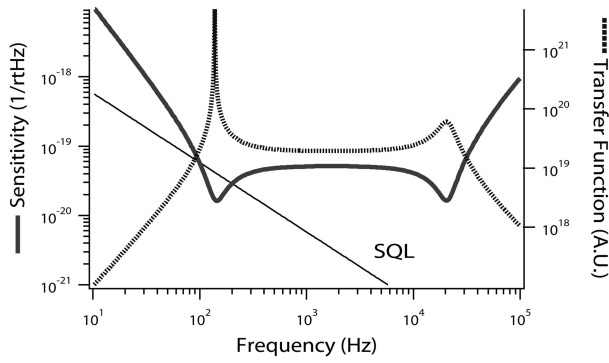


Fig. 10. Transfer function and the quantum noise level of the same detuned interferometer.

signal to the output field shown in Ref. 6 while omitting quantum noise that is sufficiently small when the mirrors are driven by a coil-magnet actuator to simulate the effect of a highly powered gravitational wave. The result is

$$|\text{transfer function}| = \frac{\sqrt{2\kappa\tau}}{h_{\text{SQL}}} \left| \frac{[1 + \rho \exp(2i\beta)] \cos \phi}{1 + \rho^2 \exp(4i\beta) - 2\rho \exp(2i\beta)[\cos 2\phi + (\kappa/2)\sin 2\phi]} \right|, \quad (6)$$

$$\beta = \arctan \frac{\Omega}{\gamma}, \quad \gamma = \frac{Tc}{4L}.$$

Here  $\phi$  is the detuning phase,  $\Omega$  is a gravitational wave frequency,  $T$  is the transmittance of the front mirrors,  $L$  is the arm length, SQL indicates the standard quantum limit, and the standard detection scheme is assumed.<sup>19</sup> The transfer function is the ratio from the differential motion of the test masses to the optical output at the signal-extraction port. As shown in Fig. 10 the transfer function of the detuned RSE has two peaks that cause the dips in the sensitivity spectrum at the corresponding frequencies.

A high-sensitivity detector is needed to observe quantum noise directly, but the transfer function can be measured with an interferometer stably locked to the detuned condition. The frequency of the lower-frequency peak depends on the laser power as<sup>6</sup>

$$\omega_{\text{low}} \approx \left[ \frac{I_0}{I_{\text{SQL}}} \frac{(2\rho\gamma^2 \sin 2\phi)(1 + 2\rho \cos 2\phi + \rho^2)}{4\rho^2 \sin^2 2\phi + (1 - \rho^2)^2} \right]^{1/2} \propto \left( \frac{I_0\gamma^2}{I_{\text{SQL}}} \right)^{1/2}, \quad (7)$$

$$I_{\text{SQL}} = \frac{mL^2\gamma^2}{4\Omega}.$$

Although we have only a 500-W laser, we can com-

pensate for the low power by using remarkably low-mass mirrors. Here  $\omega_{\text{low}}$  is proportional to the square root of  $I_0/m$  so that the peak frequency with a 200-mW laser and 40-g mirrors is the same as that with a 200-W laser and 40-kg mirrors, which is required for observing the lower peak frequency at around 100 Hz with the parameter used in the 4-m prototype. The detuning phase is chosen to be  $\phi = \pi/2 - 0.4$ .

### C. Control Scheme

We conclude that the low-low method is the most practical way to control the RSE system. In our experiment without power recycling the modulation frequency  $f_1$  is 17.25 MHz and  $f_2$  is 34.5 MHz. Although the numerical combination of  $f_1$  and  $f_2$  is a bit different from the 15–35-MHz model, this 17.25–34.5-MHz model simplifies the system since the 34.5-MHz sidebands can be generated as the second harmonics of 17.25-MHz modulation, meaning that only one modulator is necessary to generate the two sideband frequencies.

The detuned phase is chosen to be 0.4 rad from the broadband RSE. The length of the signal-recycling cavity is derived from the fact that the ratio of the free-spectral range to the frequency of the resonant RF sideband is equal to the ratio of the detuned phase ( $+2n\pi$ ) to  $2n\pi$  with an integer  $n$ , as shown in Fig. 11. Here  $n = 1$  and the ratio of the free-spectral range to the modulation frequency is defined to be  $a$ . The ratio  $a$  and the detuning phase  $\phi$  satisfy

$$\frac{a}{a-2} = \frac{2\pi}{\pi-2\phi}, \quad (8)$$

$$\frac{c}{2l_s} = a \times 17.52 \text{ MHz}; \quad (9)$$

therefore, when  $\phi = \pi/2 - 0.4$ ,

$$a = 2.292, \quad (10)$$

$$l_s = 3.794 \text{ m}. \quad (11)$$

The requirement from the optical-mode matching determines the cavity length to be 3.826 m in practice, which corresponds to a detuned phase of  $\phi = \pi/2 - 0.377$ . Also, the asymmetry for the 34.5-MHz sideband is given from Eq. (5) with  $r_p = 0$ :

$$\cos \alpha = r_s \quad (12)$$

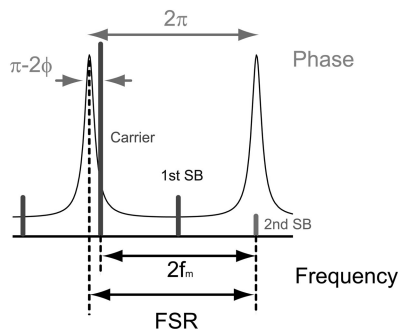


Fig. 11. FSR (equal to  $a$  times the frequency modulation) of the signal-recycling cavity determining the detuned phase. When the FSR of the signal-recycling cavity is different from the multiple of the rf SB frequency and the cavity is controlled so that one of the rf SBs is locked at the resonant point, the carrier is locked at a particular detuned condition. FSR, free-spectral range; SB, sideband.

with  $r_s = 0.89$ , so that  $\alpha = 0.47$ , then  $\Delta l = 65$  cm. The asymmetry of our RSE without power recycling should have been set to 83 cm with the consideration of optical losses included. However, the asymmetry was only 47 cm in practice since more asymmetry would cause trouble with the optical-mode matching. This decreases the magnitude of the control signal for  $\delta l_s$  by  $\sim 14\%$ .

The control signal of the signal-recycling mirror is obtained by demodulation at 51.75 MHz. The big obstruction for this scheme has been the interaction of the beat signal of the carrier and the third harmonics with the desired beat signal of the first and second sidebands. Both beat signals are extracted by demodulation at the third-harmonics frequency. The carrier light brings a large amount of information from the arm cavities; thus the interaction mixes the  $\delta l_s$  and  $\delta L_+$  signals.

One way to eliminate the influence of third harmonics is by using a secondary modulator that generates a slight number of  $3f_m$  sidebands. The output of the two modulators has a 51.75-MHz component that is proportional to  $J_3 J_0' - J_0 J_1'$ , where  $J_n$  and  $J_n'$  ( $n = 0, 1, 2, 3$ ) are the Bessel functions with the modulation depth of the first and the second modulators:  $m_1$  and  $m_2$ , respectively. It indicates that the third harmonics can be removed when the two modulation depths satisfy

$$J_3 J_0' - J_0 J_1' = 0. \quad (13)$$

In our experiment the relative phase between the modulators is matched to be  $\pi$  by adjusting the length of the cables between each modulator and the rf oscillator. Figure 12 shows the experimental result of the third-harmonics elimination. These diagrams are the outputs of the optical spectrum analyzer placed at the dark port, and each peak in the diagrams indicates the squared amplitude of the carrier and sidebands. The diagram is focused on the amount of the third-harmonics component so that the peaks of the carrier, the first sidebands, and the second sidebands

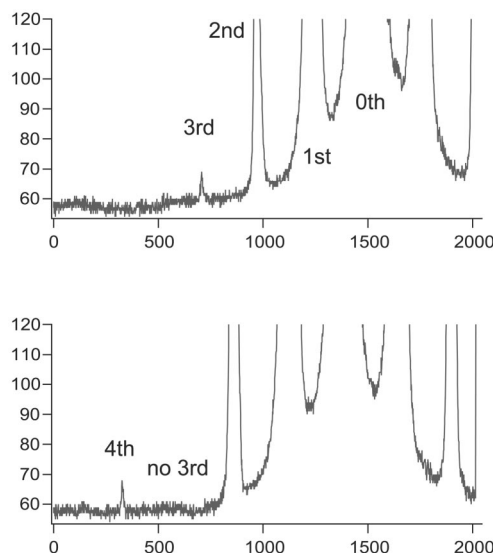


Fig. 12. Output of the optical spectrum analyzer after the modulators. Each peak indicates the intensity of the carrier and sidebands. The modulation depths of the primary (17.25-MHz) and the secondary (51.75-MHz) modulators are, top,  $m_1 = 0.63/m_2 = 0$  rad, and, bottom,  $m_1 = 0.87/m_2 = 0.07$  rad. The third-harmonic component is eliminated with an appropriate amplitude for the primary and the secondary modulations.

seem saturated. After adjustment the third-harmonics component disappears whereas the fourth component remains. Finally the modulation depths of the primary and the secondary modulators are  $m_1 = 0.87$  rad and  $m_2 = 0.07$  rad, respectively.

#### D. Operation of the Interferometer

Figure 13 shows the dc power at the dark port and the error signal of  $\delta l_s$  in the frequency domain (left) and in the XY mode (right). The numerical simulation software FINESSE is used to calculate these results.<sup>18</sup> Here the carrier is assumed not to leak through the dark port. There are six points in one periodic curve at which the error signal crosses the zero line. The interferometer can be locked to one of the points by turning on the servo. One can choose a set of broadband RSE and the  $\pm 1$ st resonant detuning or a set of broadband signal recycling and the  $\pm 2$ nd resonant detuning by choosing the polarity of the servo. Although the former three lock points have a positive slope when going from left to right, the latter three have a negative slope. The difference between the locking to the  $+1$ st and the  $-1$ st or between the  $+2$ nd and the  $-2$ nd is neglected here. The slopes at the lock points for the broadband conditions are less steep than those for the detuned conditions, so that one can choose the condition by adjusting the gain of the servo system.

By adjustment of the servo gain and the filters we are able to operate the signal-recycled Michelson interferometer locked to a detuned condition (Fig. 14). Although the original intensity of the second harmonics at the optical spectrum analyzer is  $\sim 1\%$  of the carrier, one of the second sidebands dominates when

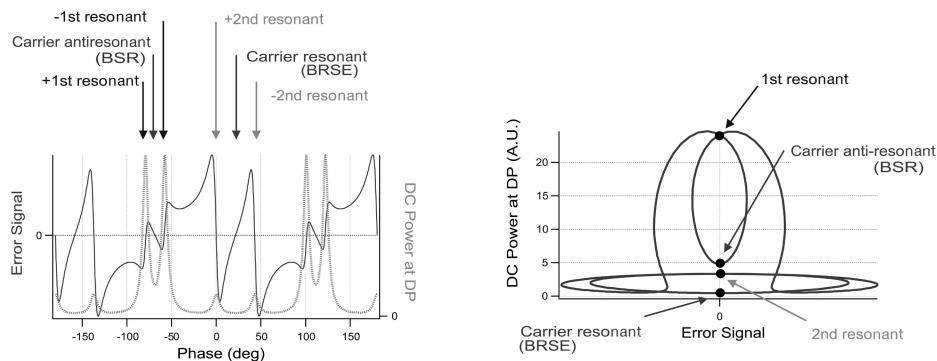


Fig. 13. Calculated error signal of  $I_s$  and the dc power at the dark port, left, with respect to the phase at the signal-recycling mirror and, right, as an X-Y plot.

the signal-recycling cavity is locked to its resonance. Because the double-demodulation signal is too weak to robustly lock the  $\delta I_s$ , we decided to use fundamental demodulation for the  $\delta I_s$  control, and the additional voltage offset is assigned to minimize the deviation from the dark fringe. Once the recycling cavity is locked, the servo system for the arm cavities can be engaged. As shown in the calculated result (Fig. 15) the error signal of the arm cavity has an offset unless the cavity is locked to the resonance when the signal-recycling cavity is locked to the detuned condition. It is important not to add a voltage offset so as to cancel the offset of the error signal, or the cavity is driven away by the supplied offset and never locked to the resonance. On the other hand, one can ascertain that the signal-recycling cavity is in a detuned condition if the transmitted light of the cav-

ity is maximized and the offset on the error signal disappears at the same moment. If the offset vanishes first and then the transmitted light is maximized, the signal-recycling cavity changes its operation point to make a broadband condition and then the arms lock under the balanced situation. To our knowledge, this is the first ever operation of the detuned RSE system with suspended mirrors in a vacuum.

Once it is whole the detuned RSE interferometer is locked, and the transfer function that could show the optical spring is ready to be measured. The sinusoidal voltage added to the feedback signal to the actuator coils drives the end mirrors differentially, simulating the gravitational waves. The differential motion appears at the connection point of the voltage and the feedback signal, being multiplied by the open-loop

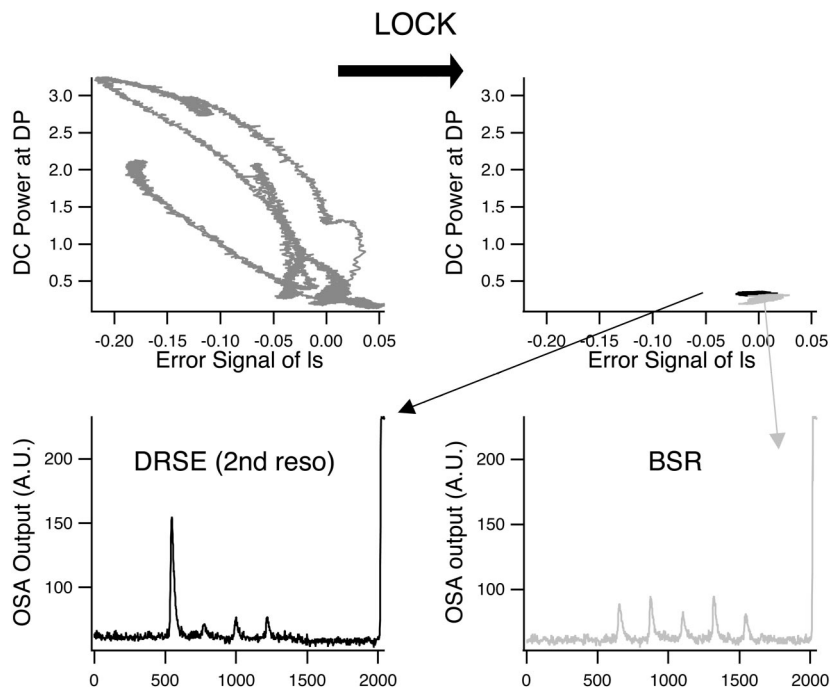


Fig. 14. Operation of a detuned RSE without the arm cavities. The upper two plots show the XY mode of the dc power at the dark port and the  $\delta I_s$  signal before and after the signal-recycling cavity is locked. The lower two are the output of the optical spectrum analyzer. In the detuned-RSE condition the largest peak is one of the second sidebands locked to the resonance.



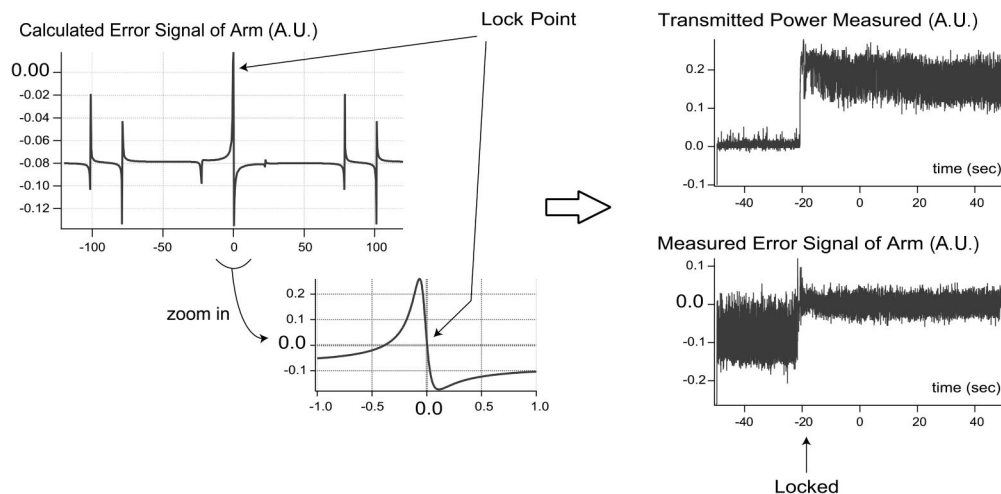


Fig. 15. Error signal of the arm cavity with an offset unless the cavity is locked to the resonance when the signal-recycling cavity is locked to the detuned condition. The experimental results agree with the condition expected from the calculation.

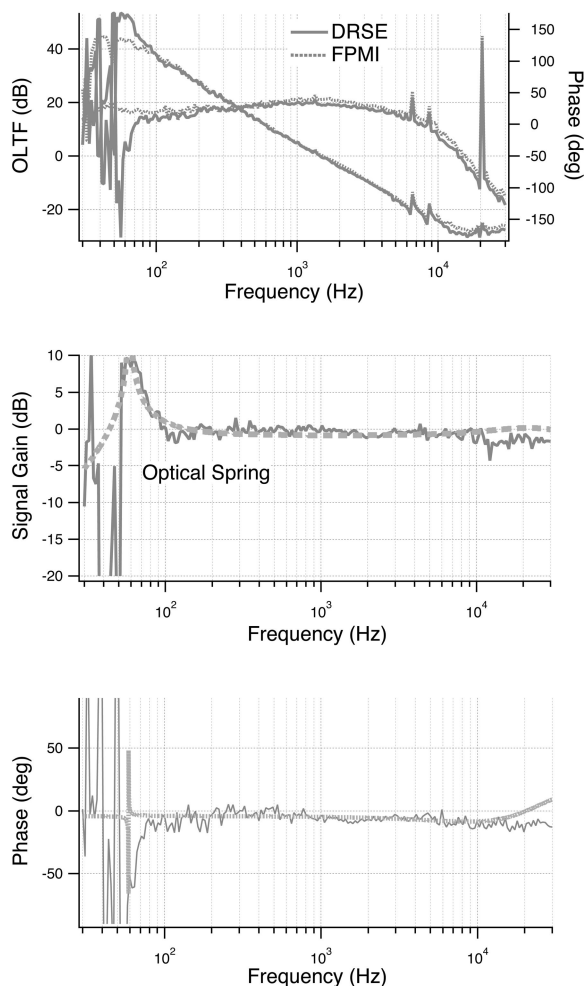


Fig. 16. Signal gain of the detuned RSE showing the optical spring at  $\sim 60$  Hz. The higher peak is hard to see probably because of the reduction in the finesse. The calculated lines are fitted to the experimental results with several parameters of the reasonable values:  $I_0 = 350$  mW,  $\mathcal{F} = 1000$ ,  $r_s = 0.4$ , and  $\phi = \pi/2 - 0.6$ .

transfer function, which includes the transfer function of the pendulum, the servo, and the interferometer. The first two components are common between the open-loop transfer function of the Fabry–Perot Michelson interferometer and the detuned RSE, so that the components can be removed by taking the ratio of these two. Figure 16 shows the final experimental result of the transfer-function measurement. The high-frequency region is covered by some structural slope, but measurement at low frequencies is remarkably improved. The result agrees with the calculated curve with the parameters:  $I_0 = 350$  mW,  $\mathcal{F} = 1000$ ,  $r_s = 0.4$ , and  $\phi = \pi/2 - 0.6$ , which shows that the loss of the mirrors has increased during the long-term observation while other properties remain constant. The reduction in finesse would have made the peak at the higher-frequency invisible in the observation band. (This assumption agrees with the fact that we were able to observe the peak at the higher frequency in the beginning of our experiment despite the presence of many environmental disturbances that were not yet removed.<sup>8</sup>) The original value of the reflectivity of the signal recycling mirror,  $r_s = 0.89$ , includes such conditions that the Michelson interferometer is perfectly locked to the dark fringe and the reflectivity of the arm cavities is much higher than that of the signal-recycling mirror. Because these conditions are not met in practice,  $r_s$  of the fitted curve appears much lower than the original value. Consequently, however, we can hopefully say that we have succeeded in observing an indication of the optical spring effect, which should be ensured with further experiments by using much higher power in the interferometer.

## 5. Conclusion

We have developed a new control scheme for an RSE interferometer that is adaptable to the second-generation, gravitational-wave detectors. The amplitude of the control signal is almost as much as that with the conventional scheme, whereas our scheme is

superior in terms of the sideband frequency not being too high. Our most significant accomplishment is achievement of the full operation of a detuned RSE interferometer with suspended mirrors by using the new control scheme. We have tried to observe the radiation-pressure effect by the transfer-function measurement and are able to see a fraction of the peaks, which should be clarified much more in the near future with the accumulation of further experiments.

We thank the members of the TAMA projects and the members of the Advanced Interferometer Configuration Committee from the LIGO Science Collaboration (LSC) for many comments. This research is supported by a grant-in-aid for Creative Basic Research of the Ministry of Education, Science, Sports, and Culture. Also we acknowledge support from a Japan Society for the Promotion of Science (JSPS) fellowship.

## References and Notes

1. M. Ando and TAMA collaboration, "Stable operation of a 300-m laser interferometer with sufficient sensitivity to detect gravitational-wave events within our galaxy," *Phys. Rev. Lett.* **86**, 3950–3954 (2001).
2. D. H. Shoemaker and the LIGO scientific collaboration, "Detector description and performance for the first coincidence observations between LIGO and GEO," *Nucl. Instrum. Methods Phys. Res. A* **517**, 154–179 (2004).
3. L. Di Fiore and the VIRGO collaboration, "The present status of the VIRGO central interferometer," *Class. Quantum Grav.* **19**, 1421–1428 (2002).
4. B. Willke, P. Aufmuth, C. Aulbert, S. Babak, R. Balasubramanian, B. W. Barr, S. Berukoff, S. Bose, G. Cagnoli, M. M. Casey, D. Churches, D. Clubley, C. N. Colacino, D. R. M. Crooks, C. Cutler, K. Danzmann, R. Davies, R. Dupuis, E. Elliffe, C. Fallnich, A. Freise, S. Gossler, A. Grant, H. Grote, G. Heinzel, A. Heptonstall, M. Heurs, M. Hewitson, J. Hough, O. Jennrich, K. Kawabe, K. Kötter, V. Leonhardt, H. Lück, M. Malec, P. W. McNamara, S. A. McIntosh, K. Mossavi, S. Mohanty, S. Mukherjee, S. Nagano, G. P. Newton, B. J. Owen, D. Palmer, M. A. Papa, M. V. Plissi, V. Quetschke, D. I. Robertson, N. A. Robertson, S. Rowan, A. Rüdiger, B. S. Sathyaprakash, R. Schilling, B. F. Schutz, R. Senior, A. M. Sintes, K. D. Skeldon, P. Sneddon, F. Stief, K. A. Strain, I. Taylor, C. I. Torrie, A. Vecchio, H. Ward, U. Weiland, H. Welling, P. Williams, W. Winkler, G. Woan, and I. Zawischa, "The GEO 600 gravitational wave detector," *Class. Quantum Grav.* **19**, 1377–1387 (2002).
5. J. Mizuno, "Comparison of optical configurations for laser-interferometric gravitational-wave detectors," Ph.D. dissertation (Max-Planck-Institute für Quantenoptik, Germany, 1995).
6. A. Buonanno and Y. Chen, "Quantum noise in second generation, signal-recycled laser interferometric gravitational-wave detectors," *Phys. Rev. D* **64**, 042006 (2001).
7. V. Braginsky and F. Khalili, *Quantum Measurement* (Cambridge University, Cambridge, England, 1992), Section 1.4.
8. K. Somiya, "Investigation of radiation pressure effect in a frequency-detuned interferometer and development of the readout scheme for a gravitational-wave detector," Ph.D. dissertation (University of Tokyo, Tokyo, Japan, 2004).
9. K. Strain, G. Müller, T. Delker, D. Reitze, D. Tanner, J. Mason, P. Willems, D. Shaddock, M. Gray, C. Mow-Lowry, and D. McClelland, "Sensing and control in dual-recycling laser interferometer gravitational-wave detectors," *Appl. Opt.* **42**, 1244–1256 (2003).
10. G. Müller, T. Delker, D. Tanner, and D. Reitze, "Dual-recycled cavity-enhanced Michelson interferometer for gravitational-wave detection," *Appl. Opt.* **42**, 1257–1268 (2003).
11. J. Mason and P. Willems, "Signal extraction and optical design for an advanced gravitational-wave interferometer," *Appl. Opt.* **42**, 1269–1282 (2003).
12. D. Shaddock, M. Gray, C. Mow-Lowry, and D. McClelland, "Power-recycled Michelson interferometer with resonant sideband extraction," *Appl. Opt.* **42**, 1283–1295 (2003).
13. O. Miyakawa, K. Somiya, G. Heintzel, and S. Kawamura, "Development of a suspended-mass RSE interferometer using third harmonic demodulation," *Class. Quantum Grav.* **19**, 1555–1560 (2002).
14. O. Miyakawa, "Development of a variable-bandwidth laser interferometer gravitational wave detector," Ph.D. dissertation (University of Tokyo, Tokyo, Japan, 2002).
15. J. Mason, "Signal extraction and optical design for an advanced gravitational wave interferometer," Ph.D. dissertation (California Institute of Technology, Pasadena, Calif., 2001).
16. B. Barr, "Experimental investigations into advanced configurations and optical techniques for laser interferometric gravitational-wave detectors," Ph.D. dissertation (University of Glasgow, Glasgow, UK, 2003).
17. P. Fritschel, "Direct-current readout for advanced LIGO," at Technical Plenary Session of the LIGO Scientific Collaboration meeting, 18–21 August 2003, Hannover, Germany, <http://www.ligo.org/>.
18. FINESSE: frequency domain interferometer simulation software is an interferometer simulation program written in C language, made by A. Freise, <http://www.rzg.mpg.de/adf/>.
19. Both the signal sidebands and the rf sidebands of a detuned RSE interferometer are not the pure phase-modulated sidebands but the unbalanced sidebands so that the readout phase, which is  $\pi/2$  for a broadband interferometer, can be chosen between 0 and  $\pi$ . Here we assume the readout phase of  $\pi/2$  as the standard detection. Further explanation is available in Chap. 5 and Appendix C of Ref. 8.